Journal of Solid State Chemistry 182 (2009) 2510–2520

Contents lists available at ScienceDirect

Journal of Solid State Chemistry

journal homepage: www.elsevier.com/locate/jssc

Uniform $AMoO_4$:Ln ($A = Sr^{2+}$, Ba^{2+}; $Ln = Eu^{3+}$, Tb^{3+}) submicron particles: Solvothermal synthesis and luminescent properties

Piaoping Yang [a], Chunxia Li [b], Wenxin Wang [a], Zewei Quan [b], Shili Gai [a], Jun Lin [b,*]

[a] College of Material Science and Chemical Engineering, Harbin Engineering University, Harbin 150001, PR China
[b] State Key Laboratory of Rare Earth Resource Utilization, Changchun Institute of Applied Chemistry, Chinese Academy of Sciences, Changchun 130022, PR China

ARTICLE INFO

Article history:
Received 16 April 2009
Received in revised form
1 July 2009
Accepted 6 July 2009
Available online 25 July 2009

Keywords:
Solvothermal synthesis
Luminescence
$BaMoO_4$
$SrMoO_4$

ABSTRACT

Rare-earth ions (Eu^{3+}, Tb^{3+}) doped $AMoO_4$ (A = Sr, Ba) particles with uniform morphologies were successfully prepared through a facile solvothermal process using ethylene glycol (EG) as protecting agent. X-ray diffraction (XRD), scanning electron microscopy (SEM), transmission electron microscopy (TEM), X-ray photoelectron spectra (XPS), Fourier transform infrared spectroscopy (FT-IR), photoluminescence (PL) spectra and the kinetic decays were performed to characterize these samples. The XRD results reveal that all the doped samples are of high purity and crystallinity and assigned to the tetragonal scheelite-type structure of the $AMoO_4$ phase. It has been shown that the as-synthesized $SrMoO_4$:Ln and $BaMoO_4$:Ln samples show respective uniform peanut-like and oval morphologies with narrow size distribution. The possible growth process of the $AMoO_4$:Ln has been investigated in detail. The EG/H_2O volume ratio, reaction temperature and time have obvious effect on the morphologies and sizes of the as-synthesized products. Upon excitation by ultraviolet radiation, the $AMoO_4$:Eu^{3+} phosphors show the characteristic $^5D_0$–$^7F_{1-4}$ emission lines of Eu^{3+}, while the $AMoO_4$:Tb^{3+} phosphors exhibit the characteristic $^5D_4$–$^7F_{3-6}$ emission lines of Tb^{3+}. These phosphors exhibit potential applications in the fields of fluorescent lamps and light emitting diodes (LEDs).

1. Introduction

During the past decades, self-assembled micrometer-sized inorganic materials with special size, morphology, and hierarchy were of special interest in the areas of materials synthesis and device fabrication due to their hierarchical and repetitive superstructures, which show potential applications in wide fields of crystals, catalysis, diagnostics, and pharmacology [1–8]. Considerable efforts have been devoted to the synthesis of two-dimensional (2-D) and three-dimensional (3-D) microscale particles with well-controlled morphology and architectures for revealing their morphology-dependent properties and for achieving their promising applications, because of their unique optical, electronic, magnetic, and mechanical properties [9–13]. 3-D hierarchical particles have attracted special attention because of the practical importance related to some fractal growth process. In most cases, the formation of 3-D hierarchical particles may result from the evolution of 1-D primary crystals via an oriented routine or a self-assembly process, which results in the formation of anisotropic shapes arising from the blocking or retarding of growth along one or more directions through selective adhesion [14–19]. Furthermore, because the physicochemical properties of crystals depend not only on their chemical composition but also on the morphology and size, controllable synthesis of high-ordered structures then is very intriguing. So far, various approaches have been employed to control the shape and size of the products, such as template methods [20,21], vapor transport and condensation [22], Langmuir–Blodgett technology [23,24], chemical vapor deposition (CVD) [25], and electrodeposition method [26].

Metal molybdates of relatively large bivalent cations ($AMoO_4$, ionic radius >0.99 Å, A = Ca, Ba, Sr) mainly exist in a scheelite-type tetragonal structure form, where the molybdenum atom adopts tetrahedral coordination [27]. Recently, metal molybdates such as $SrMoO_4$ and $BaMoO_4$ have been extensively studied or reviewed due to their luminescent behavior and structural properties, which have potential application as electro-optical device, solid-state laser, photoluminescence device, scintillators, acousto-optic filter, and stimulated Raman scattering materials [28–37]. Flux method [38], Czochralski technique [39], floating zone-like technique [40], co-precipitation process [41], citrate complex method [42], hydrothermal technique [43,44], and solvothermal routines [45–47] have been employed to prepare molybdates. Among all these methods, surfactant-assisted microemulsion-mediated solvothermal process has proved an efficient approach to synthesize inorganic materials with interesting morphologies and regular particle sizes. However, in the reverse micelles and microemulsion process, the introduction of templates or substrates usually results in heterogeneous impurities,

* Corresponding author. Fax: +86 431 85698401.
E-mail address: jlin@ciac.jl.cn (J. Lin).

0022-4596/$ - see front matter © 2009 Elsevier Inc. All rights reserved.
doi:10.1016/j.jssc.2009.07.009

which increases the production cost for further treatment, leading to the difficulty for scale-up production. Thus, the seeking of facile process for the synthesis of inorganic materials with controllable features without using the surfactants should be of significant promise.

Furthermore, many rare-earth ions (Eu^{3+}, Tb^{3+}) doped scheelite-related molybdates have been reported and have broad and intense absorption bands due to charge transfer (CT) from oxygen to metal in the near-UV region [48,49]. It is shown that $CaMoO_4:Eu^{3+}$ can be effectively excited by near-UV LEDs (380–410 nm), and then emits bright red fluorescence ($^5D_0$–$^7F_2$). Therefore, rare-earth-ions-doped molybdates should be potential materials for LED applications. To the best of our knowledge, the solvothermal process using ethylene glycol (EG) as reaction media for the synthesis of the rare-earth-ions-doped molybdates without further heat treatment has never been reported. Herein, a facile solvothermal process using EG as protective agent without templates was proposed for the synthesis of rare-earth ion (Eu^{3+}, Tb^{3+})-doped molybdates particles with uniform morphology and narrow size distribution. The obtained samples were well characterized by means of XRD, FESEM, TEM, XPS, IR, optical spectra as well as the kinetic decay times. A possible growth process for the micro-sized particles has also been investigated.

2. Experimental section

2.1. Synthesis of SrMoO4:Eu^{3+}, $SrMoO_4:Tb^{3+}$, $BaMoO_4:Eu^{3+}$, and $BaMoO_4$: Tb^{3+}

All the reagents for synthesis including ethylene glycol (EG) (A. R., Beijing Fine Chemical Company), $Sr(NO_3)_2$ and $Ba(NO_3)_2$ (A. R., Beijing Chemical Regent Company), ammonium molybdate ($(NH_4)_6Mo_7O_{24}\cdot 4H_2O$) (A. R., Beijing Chemical Regent Company), Eu_2O_3, Tb_4O_7 (99.99%, Science and Technology Parent Company of Changchun Institute of Applied Chemistry), HNO_3 (A. R., Beijing Beihua Chemical Company) were used without further purification. The doping concentration of Eu^{3+} was 5 mol% to Sr^{3+} in $SrMoO_4:Eu^{3+}$. In a typical process, 0.0176 g (0.05 mmol) of Eu_2O_3 was dissolved in dilute HNO_3 with stirring. The superfluous HNO_3 was driven off until the pH value of the solution reached between 2 and 3. The obtained $Eu(NO_3)_3$ crystal powders and 0.201 g (0.95 mmol) of $Sr(NO_3)_2$ were added into 20 mL of the mixed solution of EG and water (volume ratio = 37/3) under stirring. Another 20 mL of the same solution containing 0.176 g of $(NH_4)_6Mo_7O_{24}\cdot 4H_2O$ were added to the former solution. After further stirring for another 1 h, the resulting solution was then transferred into a 50 mL sealed Teflon autoclave and statically heated at 160 °C for 8 h. After the autoclave was naturally cooled to room temperature, the final products were separated by centrifugation, and washed several times with ethanol and distilled water. Finally, the obtained samples were dried in vacuum at 80 °C for 24 h. In this way, the Eu^{3+}-doped $SrMoO_4$ was obtained, which was designated as $SrMoO_4:Eu^{3+}$. $SrMoO_4:Tb^{3+}$ with the doping concentration of 5 mol% of Tb^{3+} and $BaMoO_4:Eu^{3+}$ (Tb^{3+}) with the doping concentration of 5 mol% of Eu^{3+} (Tb^{3+}) were prepared in the same process.

2.2. Characterization

Powder XRD patterns were obtained on a Rigaku TR III diffractometer with Cu$K\alpha$ radiation ($\lambda = 0.15405$ nm). The accelerating voltage and emission current are 40 kV and 200 mA, respectively. Fourier-Transform IR spectra were performed on a Perkin-Elmer 580B IR spectrophotometer using the KBr pellet technique. Field emission scanning electron microscope (FESEM) images were inspected on an XL30 microscope (Philips) equipped with an energy-dispersive X-ray spectrum (EDS, JEOL JXA-840). Transmission electron microscope (TEM) and high-resolution transmission electron microscope (HRTEM) images were carried out on an FEI Tecnai G^2 S-Twin with an acceleration voltage of 200 kV. The samples used for TEM were prepared by dispersing some products in ethanol, then placing a drop of the solution onto a copper grid and letting the ethanol evaporate slowly in air. The X-ray photoelectron spectra (XPS) were taken on a VG ESCALAB MK II electron energy spectrometer using Mg$K\alpha$ (1253.6 eV) as the X-ray excitation source. The doping concentrations of Eu^{3+} and Tb^{3+} in the resulting materials were determined by Inductively Coupled Plasma (ICP) (ICP–PLASMA 1000). The UV–vis excitation and emission spectra were recorded on a Hitachi F-4500 spectrofluorimeter equipped with a 150 W xenon lamp as the excitation source. Luminescence decay curves were obtained from a Lecroy Wave Runner 6100 Digital Oscilloscope (1 GHz) using a 250 nm laser (pulse width = 4 ns, gate = 50 ns) as the excitation source (Continuum Sunlite OPO). All the measurements were performed at room temperature.

3. Results and discussion

3.1. Phase, composition and structure

The phase and the composition of the rare-earth-ions-doped $SrMoO_4$ samples were first examined by XRD, as shown in Fig. 1. The vertical bars (Fig. 1c) indicate a standard tetragonal bulk $SrMoO_4$ peak position from the standard data (JCPDS 08–0482). It

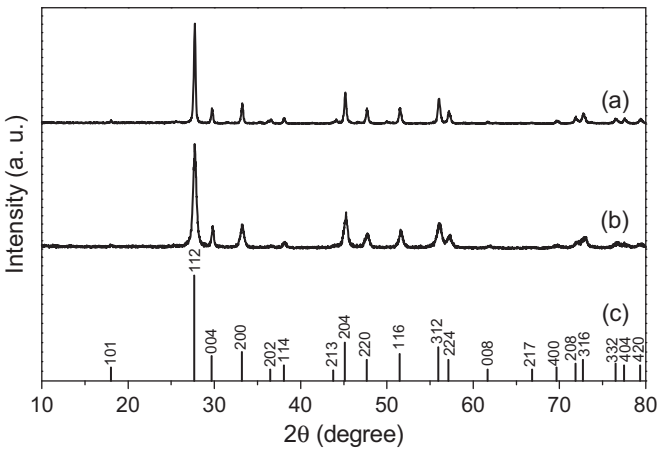

Fig. 1. XRD patterns of the as-synthesized $SrMoO_4:Eu^{3+}$ (a), $SrMoO_4:Tb^{3+}$ (b), and the standard data for bulk $SrMoO_4$ (JCPDS 08–0482) (c).

Table 1
Unit-cell parameters and the deviations for the as-synthesized $SrMoO_4:Eu^{3+}$, $SrMoO_4:Tb^{3+}$, $BaMoO_4:Eu^{3+}$, and $BaMoO_4:Tb^{3+}$ samples.

Samples	*a*, *b* (Å)/ deviations	*c* (Å)/ deviations	Unit cell volume (Å^3)/deviations	Crystal size (nm)
JCPDS 08–0482	5.394	12.01	3.492	
$SrMoO_4:Eu^{3+}$	5.382/0.012	11.98/0.03	3.469/0.023	19
$SrMoO_4:Tb^{3+}$	5.386/0.008	11.99/0.02	3.477/0.015	21
JCPDS 29–0193	5.580	12.821	3.992	
$BaMoO_4:Eu^{3+}$	5.567/0.013	12.790/0.031	3.964/0.028	23
$BaMoO_4:Tb^{3+}$	5.570/0.010	12.801/0.02	3.979/0.013	25

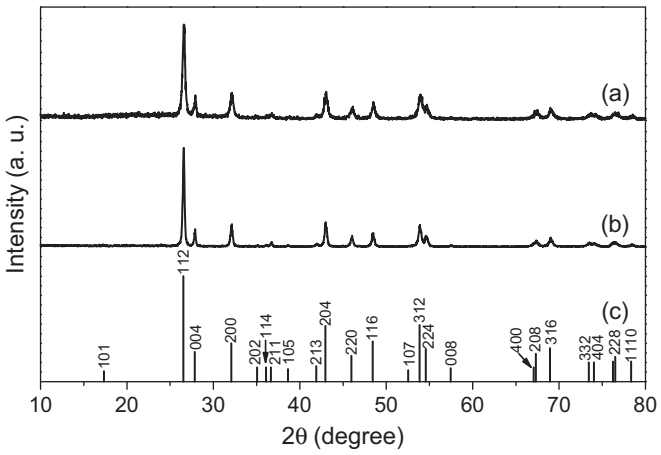

Fig. 2. XRD patterns of the as-synthesized $BaMoO_4:Eu^{3+}$ (a), $BaMoO_4:Tb^{3+}$ (b), and the standard data for bulk $BaMoO_4$ (JCPDS 29–0193) (c).

can obviously be found that all the XRD diffractions of the products can be well indexed as a pure tetragonal phase ($I4_1/a$ space group), agreeing well with the values of the standard card. No other impurities related to doped components can be detected, suggesting the high purity of the samples and that rare-earth ions have been uniformly incorporated into the host lattice of $SrMoO_4$. The calculated unit-cell parameters of the as-synthesized samples (Table 1) are well consistent with the standard data (JCPDS 08–0482). Furthermore, it is clear that the diffractions of the XRD patterns show some distant broadening, indicating the small size nature of the components. The peak broadening can be used to estimate the average crystallite sizes by the Scherrer formula, $D = 0.89\lambda/\beta\cos\theta$, where D is the average grain size, λ is the X-ray wavelength (0.15405 nm), and θ and β are the diffraction angle and full-width at half-maximum (FWHM), respectively. The strongest three peaks (112) at $2\theta = 27.66^\circ$, (204) at $2\theta = 45.11^\circ$, and (312) at $2\theta = 55.95^\circ$ were used to calculate the average crystallite size (D) of the sample. The average crystallite sizes for $SrMoO_4:Eu^{3+}$ and $SrMoO_4:Tb^{3+}$ were finally estimated be about 19

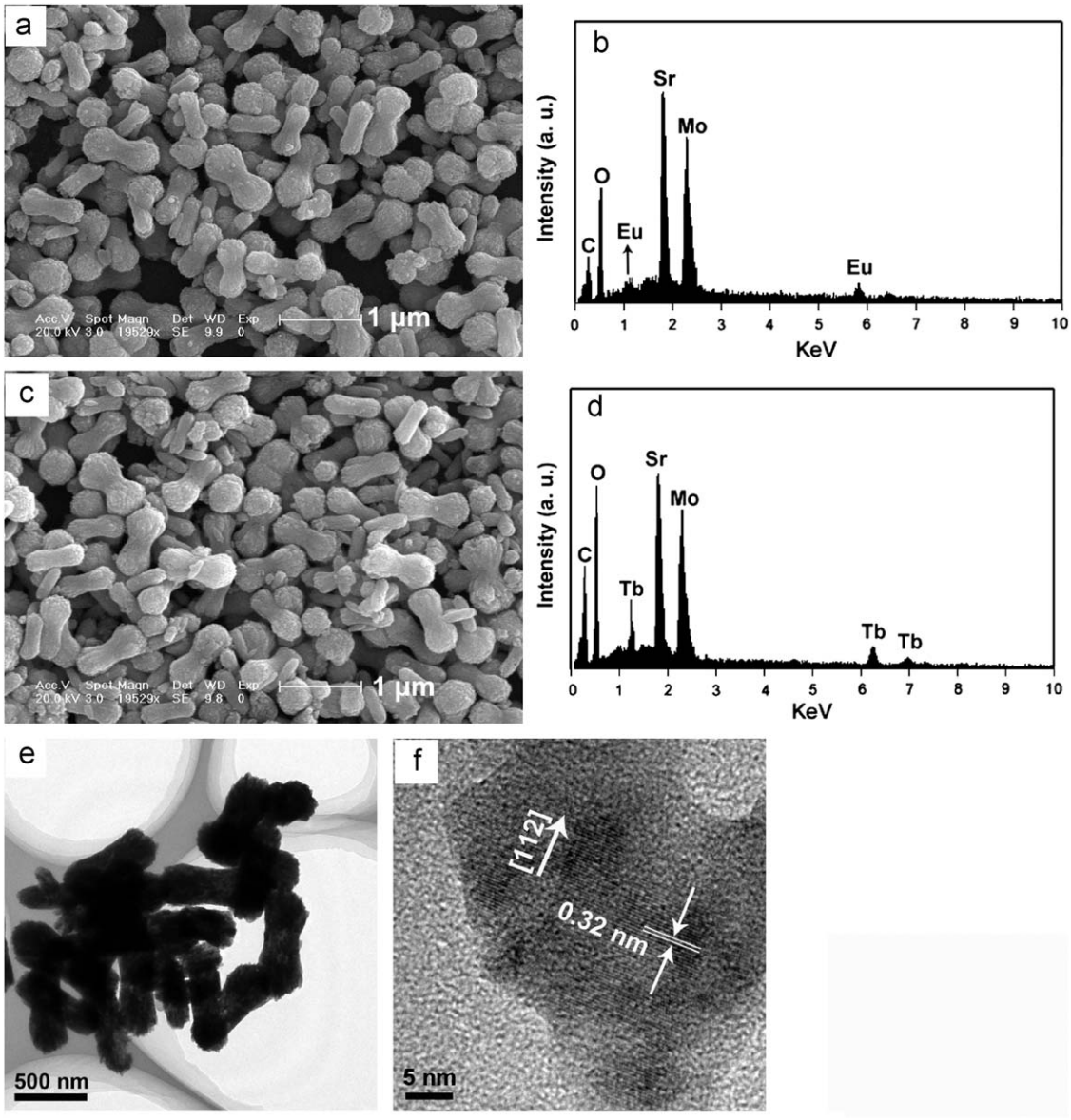

Fig. 3. SEM image of $SrMoO_4:Eu^{3+}$ (a), EDS of $SrMoO_4:Eu^{3+}$ (b), SEM image of $SrMoO_4:Tb^{3+}$ (b), EDS of $SrMoO_4:Tb^{3+}$ (d), TEM (e), and HRTEM (f) images of the $SrMoO_4:Eu^{3+}$ sample synthesized at 160 °C for 8 h.

and 21 nm, as shown in Table 1. Moreover, the respective actual doping concentrations of Eu^{3+} in $SrMoO_4$:Eu^{3+} and of Tb^{3+} in $SrMoO_4$:Tb^{3+} sample are 2.98 and 3.09 wt% as determined by the ICP analysis, which are much closer to the stoichiometric values (3.03 wt% or 5 mol% to Sr^{2+} in $SrMoO_4$:Eu^{3+} and 3.16 wt% or 5 mol% to Sr^{2+} in $SrMoO_4$:Tb^{3+}).

Fig. 2 gives the XRD patterns of rare-earth-ions-doped $BaMoO_4$ samples and the standard data for the tetragonal $BaMoO_4$, respectively. The diffraction peaks can be directly indexed to the tetragonal $BaMoO_4$ in $I4_1/a$ space group (JCPDS 29–0193). The calculated cell lattice constants summarized in Table 1 are in good agreement with the standard values of pure $BaMoO_4$, indicating the high purity and crystallinity of the as-synthesized samples. Moreover, the average crystallite sizes determined by the Scherrer formula are calculated to be 23 and 25 nm, respectively. The actual doping concentrations of Eu^{3+} and Tb^{3+} in the doped $BaMoO_4$ products are 2.49 and 2.58 wt%, respectively, as determined by ICP analysis, which are similar to the stoichiometric values (2.54 and 2.66 wt% or 5 mol% to Ba^{2+} in $BaMoO_4$:Eu^{3+} and $BaMoO_4$:Tb^{3+}).

3.2. Morphology

The morphology and the microstructure details of the as-synthesized products were examined by SEM and TEM techniques. Fig. 3 shows the SEM images, EDS of $SrMoO_4$:Eu^{3+} and $SrMoO_4$:Tb^{3+}, TEM and the HRTEM images of $SrMoO_4$:Eu^{3+}. The low-magnification SEM image (Fig. 3a and c) reveals that the two as-synthesized products consist of exclusively peanut-like particles with relatively narrow size distribution, indicating that the doping components have little effect on the morphological features of the samples. Additionally, the samples exhibit relatively well-defined peanut-like crystals with diameter 300–500 nm and length 800–1000 nm. Furthermore, it can be seen that the single peanut-like particle is actually composed of numerous small nanosized particles, which can be responsible for the broadening of the XRD peaks. The EDS (Fig. 3b and d) of the samples confirms the presence of strontium (Sr), molybdenum (Mo), oxygen (O), europium (Eu), and terbium (Tb) in the product (the carbon signal is from the carbon substrate). The approximate surface composition extracted from the EDS analysis gives a

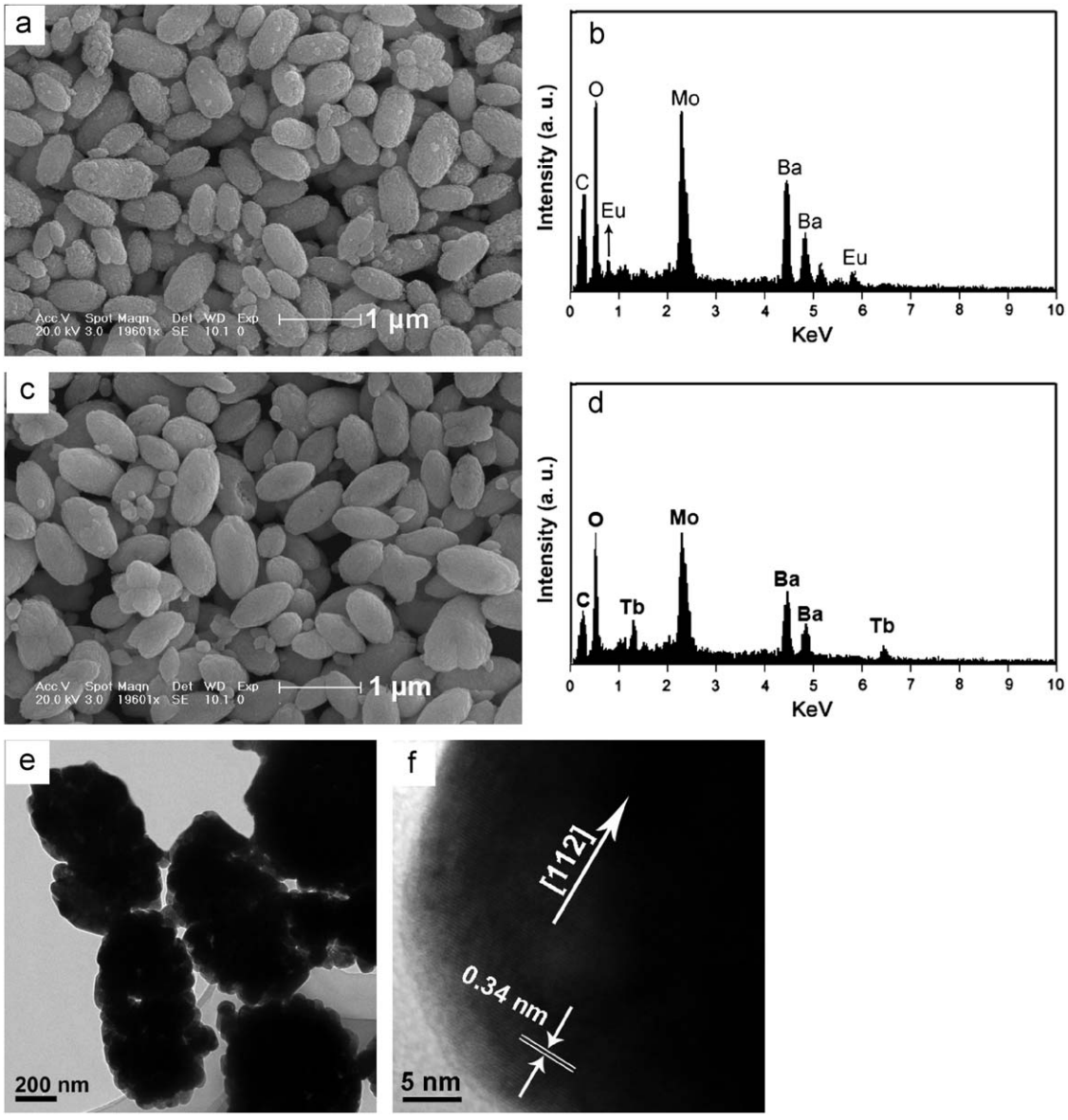

Fig. 4. SEM image of $BaMoO_4$:Eu^{3+} (a), EDS of $BaMoO_4$:Eu^{3+} (b), SEM image of $BaMoO_4$:Tb^{3+} (c), EDS of $BaMoO_4$:Tb^{3+} (d), TEM (e), and HRTEM (f) images of the $BaMoO_4$:Eu^{3+} sample synthesized at 160 °C for 8 h.

Eu/Sr/Mo/O atomic ratio of 0.04:0.96:1:4.1, which is much closer to the ICP results. TEM investigations can provide further insight into the morphology details and structural features of the peanut-like particles. The TEM image (Fig. 3e) of $SrMoO_4:Eu^{3+}$ exhibits much similar morphological features provided by the SEM analysis. Furthermore, the lattice fringes in the HRTEM image (Fig. 3f) are obvious, revealing the high crystallinity of the product. The lattice fringes of (112) planes with an interplanar distance of 0.32 nm are marked by the arrows. The calculated interplanar distance between the adjacent lattice fringes agrees well with the d_{112} spacing of the literature value (0.3222 nm) (JCPDS 08–0482). HRTEM investigation confirms the high crystallinity and single-crystal nature of the product.

The typical SEM images, EDS of $BaMoO_4:Eu^{3+}$ and $BaMoO_4:Tb^{3+}$, TEM and the HRTEM images of $BaMoO_4:Eu^{3+}$ are depicted in Fig. 4. It can be seen that the two samples are composed of uniform oval particles with the particle size of about 1 μm in length and 300–500 nm in width (Fig. 4a and c). These particles are non-aggregated with narrow size distribution. The SEM image also reveals that the big single particle actually consists of many small nanoparticles, which results in the broadening of the XRD patterns. In the EDS spectra (Fig. 4b and d), the signals of barium (Ba), molybdenum (Mo), oxygen (O), europium (Eu), and terbium (Tb) suggest the presence of the corresponding element in the products (the carbon signal is due to the carbon used). The EDS analysis gives the approximate surface composition of 0.06/0.94/0.9/4.0 of Eu/Ba/Mo/O molar ratio in the as-synthesized product, agreeing well with the ICP results. The TEM image (Fig. 4e) shows a morphology similar to that of the SEM result. In this HRTEM image (Fig. 4f), taken with the electron beam perpendicular to the *c*-axis of the oval particle, the interplanar distances between adjacent lattice fringes are determined as 0.34 nm, agreeing well with the *d* spacing value (0.3357 nm) of the (112) planes of tetragonal $BaMoO_4$.

The surface components of $SrMoO_4:Eu^{3+}$ and $BaMoO_4:Eu^{3+}$ were further examined by the XPS analysis, as shown in Fig. 5. In the XPS spectrum of $SrMoO_4:Eu^{3+}$ (Fig. 5a), the binding energy (calibrated using C 1 s (284.7 eV) as the reference) of Mo ($Mo2p_{3/2}$, 415.1 eV; $Mo2p_{1/2}$, 398 eV; $3d_{5/2}$, 232.5 eV; $3d_{3/2}$, 235.3 eV), Eu (3*d*, 1132.9 eV), O (1*s*, 529.6 eV), and Sr (2*p*, 132.9 eV) can be obviously found (the C signal is due to the carbon used as reference). By combining the XRD result, it can be deduced that these signals can be attributed to $SrMoO_4:Eu^{3+}$. In the case of $BaMoO_4:Eu^{3+}$ (Fig. 5b), in addition to the binding energies of Mo, O, and Eu, the binding energies of Ba ($Ba2p_{3/2}$, 778.1 eV; $Ba2p_{1/2}$, 793.4 eV) are apparent.

Fig. 6 shows the FT-IR spectra of the as-synthesized $SrMoO_4:Eu^{3+}$ and $BaMoO_4:Eu^{3+}$ particles synthesized at 160 °C for 8 h. It can be seen that the two samples have approximate vibration modes. The respective bands at 3419 and 1631 cm^{-1} can be ascribed to O–H stretching vibration and H–O–H bending vibration of physically absorbed water on the sample surface. A strong absorption peak at 807 cm^{-1} can be assigned to ν_3 anti-symmetric stretching vibration originating from the Mo–O stretching vibration in MoO_4^{2-} tetrahedron [44,50]. And the weak adsorption peak at 404 cm^{-1} can be assigned to ν_2 bending vibration of Mo–O [44]. C–H_x bending vibration at 2921 cm^{-1} can be detected, indicating the incomplete removal of the EG molecules from the surface of the samples.

3.3. *The growth process and the factors influencing the formation of the products*

A proposed formation process is presented in Scheme 1. Typically, after the two solutions containing $Sr(NO_3)_2$ and

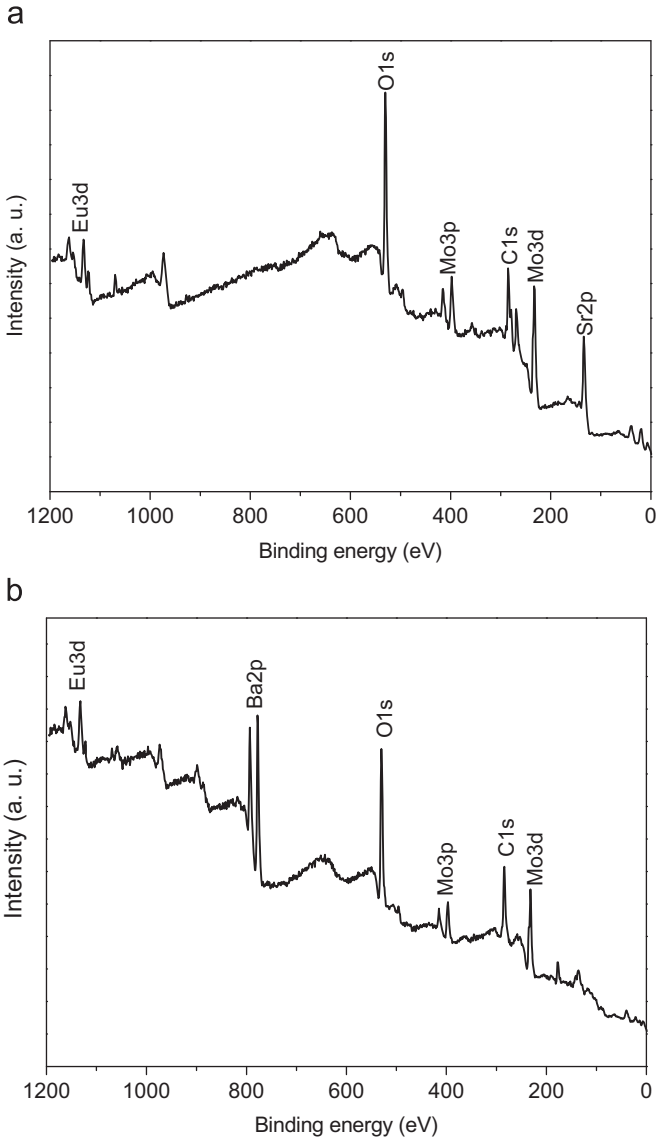

Fig. 5. XPS spectra for the as-synthesized $SrMoO_4:Eu^{3+}$ and $BaMoO_4:Eu^{3+}$ phosphors.

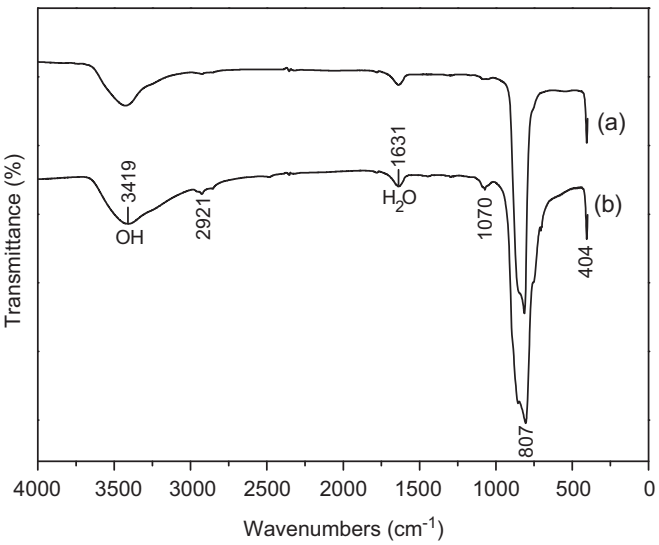

Fig. 6. FT-IR spectra of the as-synthesized $SrMoO_4:Eu^{3+}$ and $BaMoO_4:Eu^{3+}$ samples synthesized at 160 °C for 8 h.

$(NH_4)_6Mo_7O_{24}\cdot 4H_2O$ were mixed together, amorphous $SrMoO_4$ nuclei will form. When the water ratio in the media is very low and the EG concentration is high enough, the low water content in the media leads to the formation of numerous tiny droplets surrounded by the protective agent. The amorphous fine particles may act as the precursor and the subsequent growth of $SrMoO_4:Eu^{3+}$ nuclei is confined within the droplets. Consequently, the peanut-like $SrMoO_4:Eu^{3+}$ crystals were formed by self-assembly through the further solvothermal process. The formation of $BaMoO_4:Tb^{3+}$ proceeds in a routine similar to that of $SrMoO_4:Eu^{3+}$ except for the oval morphology of the final product. In order to investigate the formation process, pure water was used as the reaction media for the synthesis of the same product through a hydrothermal process. Ethylene glycol (EG) has been widely used as an effectively protective agent to control the growth rate of the particles in the solvothermal process. Thus, the size and morphology of the final products should be much different when using different concentrations of water and EG in the reaction media. Fig. 7 shows the typical SEM images of the as-synthesized $SrMoO_4:Eu^{3+}$ particles synthesized with EG/H_2O volume ratios of 0 and 37/3, respectively. FE-SEM micrographs obviously reveal that the $SrMoO_4:Eu^{3+}$ powders synthesized at 160 °C for 8 h with EG/H_2O volume ratio of 0 (pure water) exhibit a large quantity of small particles with agglomerated and polydisperse features (Fig. 7a). This random aggregation can be related to the increase of the effective collision rates between the nano-scale particles by the hydrothermal treatment without the protection of the EG molecules [51]. In the case of the sample synthesized with the EG/H_2O volume ratio of 37/3, the high magnification image (Fig. 7b) indicates the relatively uniform peanut-like morphologies with the particle size of 800–1000 nm in length and 300–500 nm in width. It can be obviously seen that the large particles actually consist of numerous nanosized small particles. The adsorption/absorption of a large amount of EG molecules on the surface of the small particles and the high collision rates promoted by the solvothermal treatment favor the formation of the peanut-like morphology. The results indicate that the volume ratio of EG/H_2O play a key role in affecting the morphology and size of the final product.

To further study the growth of $SrMoO_4:Eu^{3+}$ and $BaMoO_4:Tb^{3+}$ microcrystals in the solvothermal process, the products synthesized at different solvothermal times and temperatures were investigated in detail using the FE-SEM technique. Fig. 8 shows the SEM images of $SrMoO_4:Eu^{3+}$ synthesized at different temperatures of 140, 160, 180 and 200 °C for 8 h with the EG/H_2O volume ratio of 37/3. Obviously, the particle size of the samples shows a gradually increasing trend from 500 nm to 1 μm in length with the increasing reaction time from 4 to 24 h, while the relatively uniform peanut-like morphology has been maintained. Of note is that when the reaction temperature is increased to 200 °C, the microproducts did not have the exclusive peanut-like morphology, and some nanoparticles with much smaller particle size are also found (Fig. 8d). The typical SEM image of $SrMoO_4:Eu^{3+}$ synthesized at 160 °C for different reaction times is given in Fig. 9. An obvious growing process from the small

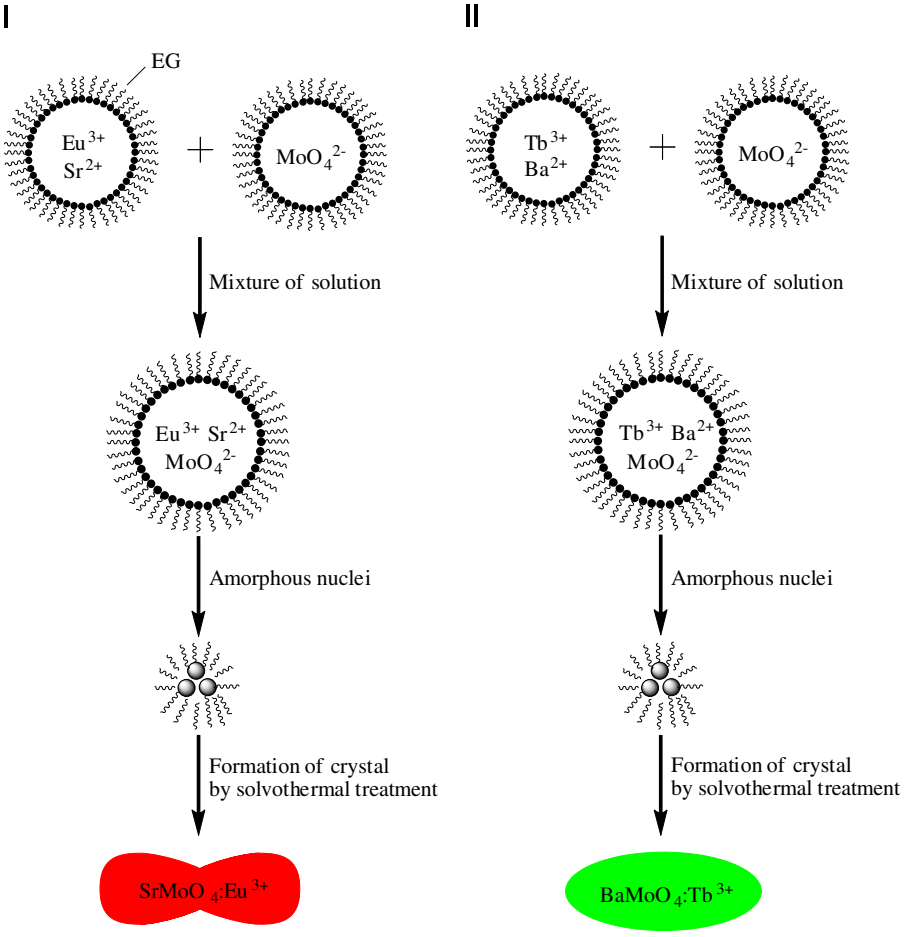

Scheme 1. Illustration for the formation process of $SrMoO_4:Eu^{3+}$ and $BaMoO_4:Tb^{3+}$ with different morphologies.

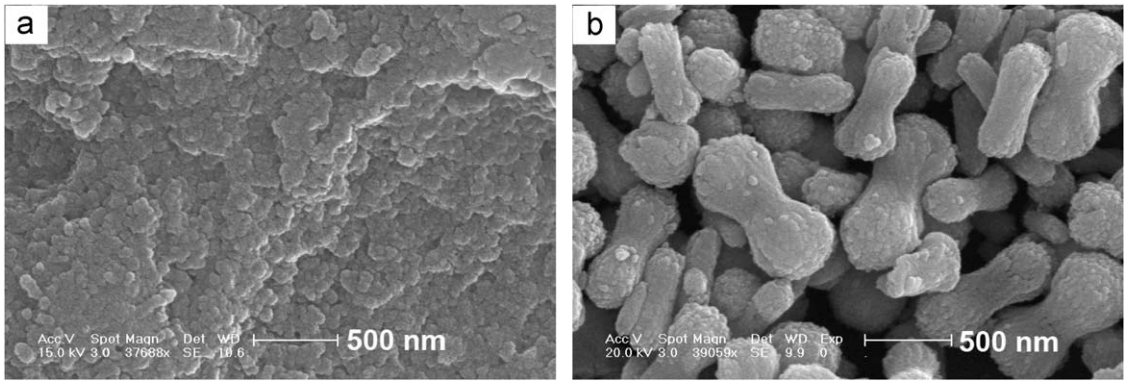

Fig. 7. SEM images of the as-synthesized $SrMoO_4:Eu^{3+}$ particles synthesized with EG/H_2O volume ratio of 0 (a) and 37/3 (b) at 160 °C for 8 h.

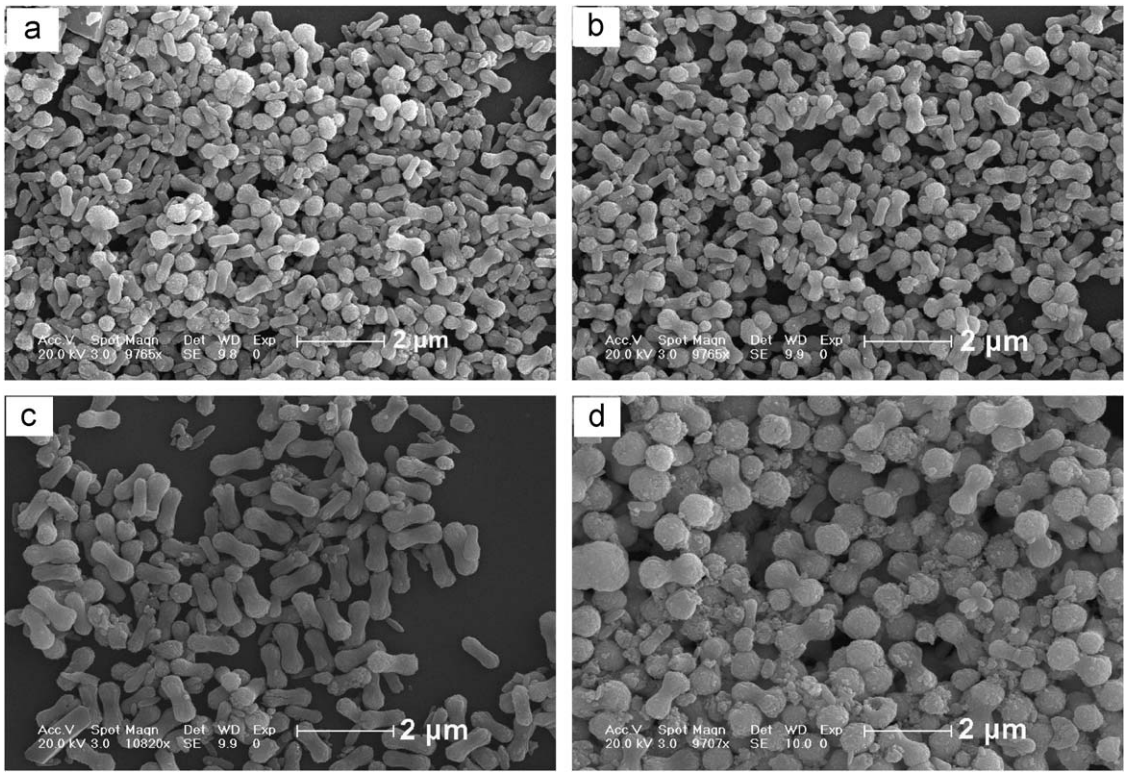

Fig. 8. SEM images of the as-synthesized $SrMoO_4:Eu^{3+}$ particles synthesized at 140 °C (a), 160 °C (b), 180 °C (c), and 200 °C (d) for 8 h.

particle to the final larger products by self-assembly is found. The results suggest that the reaction temperature and time play an important role in the morphology and size of the final product. A similar growth process has also been found for the formation of $BaMoO_4:Tb^{3+}$ synthesized at different temperatures, except for the oval morphology of the products (Fig. 10).

3.4. Photoluminescence properties

The as-synthesized $SrMoO_4:Eu^{3+}$ and $BaMoO_4:Eu^{3+}$ particles show red emission under ultraviolet (254 nm) excitation, as shown in Fig. 11. The PL properties of the samples were further characterized by the PL excitation and emission spectra (Fig. 11a and b). It can be seen that the two Eu^{3+}-doped samples show much similar PL spectra. The excitation spectra were obtained by monitoring the emission of the Eu^{3+} $^5D_0$–$^7F_2$ transition at 612 nm. It is obvious that all the spectra consist of a broad band with a maximum at about 270 nm and some weak peaks between 300 and 500 nm. The broad band at 270 nm can be associated with the MoO_4^{2-} groups [52]. The weak peaks within the Eu^{3+} $4f^6$ configuration can be assigned to $^7F_0 \rightarrow {}^5D_4$ (367 nm), $^7F_0 \rightarrow {}^5L_6$ (396 nm) and $^7F_0 \rightarrow {}^5D_2$ (469 nm) [53]. Upon excitation into the MoO_4^{2-} groups at 270 nm, not only the characteristic transition lines from the lowest excited $^5D_0$ but also those from higher energy levels ($^5D_1$) with weak intensities can be found (Fig. 11a and b, right) (the locations of the emission lines together with their assignments are labeled as well) [54]. The emission of Eu^{3+} is dominated by the red $^5D_0$–$^7F_2$ hypersensitive transition.

As shown in Fig. 11, the as-synthesized $SrMoO_4:Tb^{3+}$ and $BaMoO_4:Tb^{3+}$ particles show green emission under short ultraviolet (254 nm) excitation. Fig. 11(c and d) depicts the PL excitation and emission spectra of the $SrMoO_4:Tb^{3+}$ and $BaMoO_4:Tb^{3+}$ particles, respectively. The two samples also show

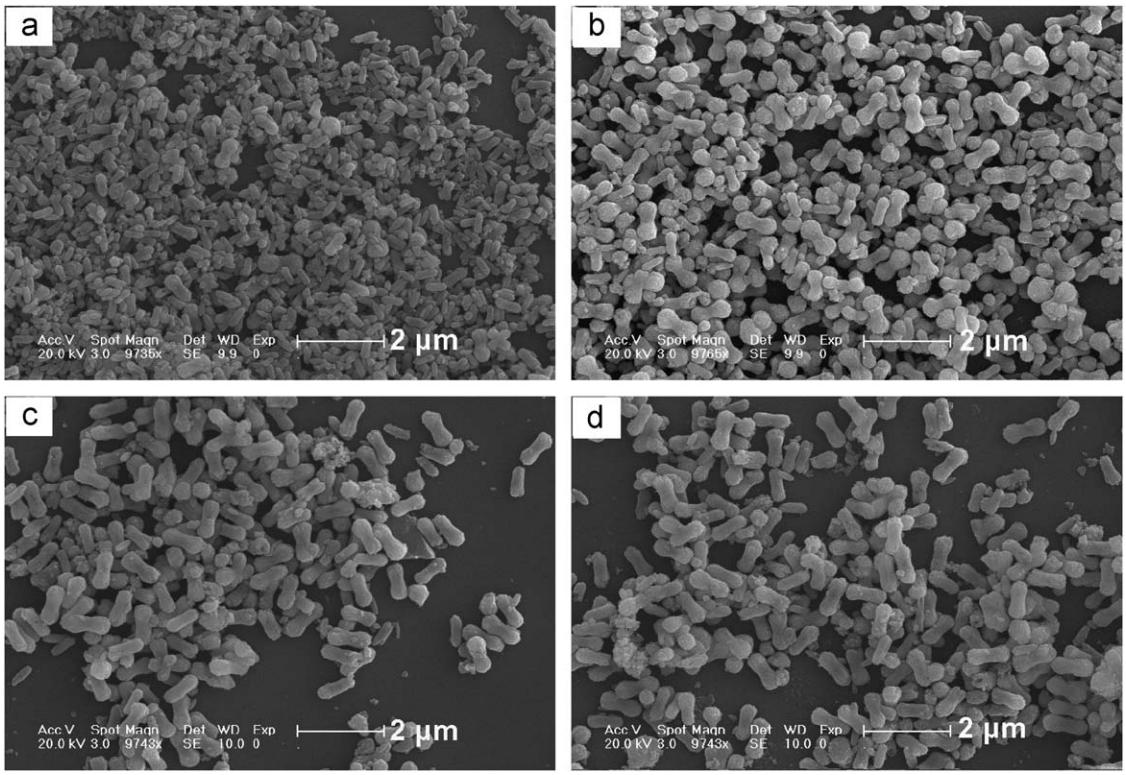

Fig. 9. SEM images of the as-synthesized $SrMoO_4:Eu^{3+}$ particles synthesized at 160 °C for 4 h (a), 8 h (b), 12 (c), and 24 (h).

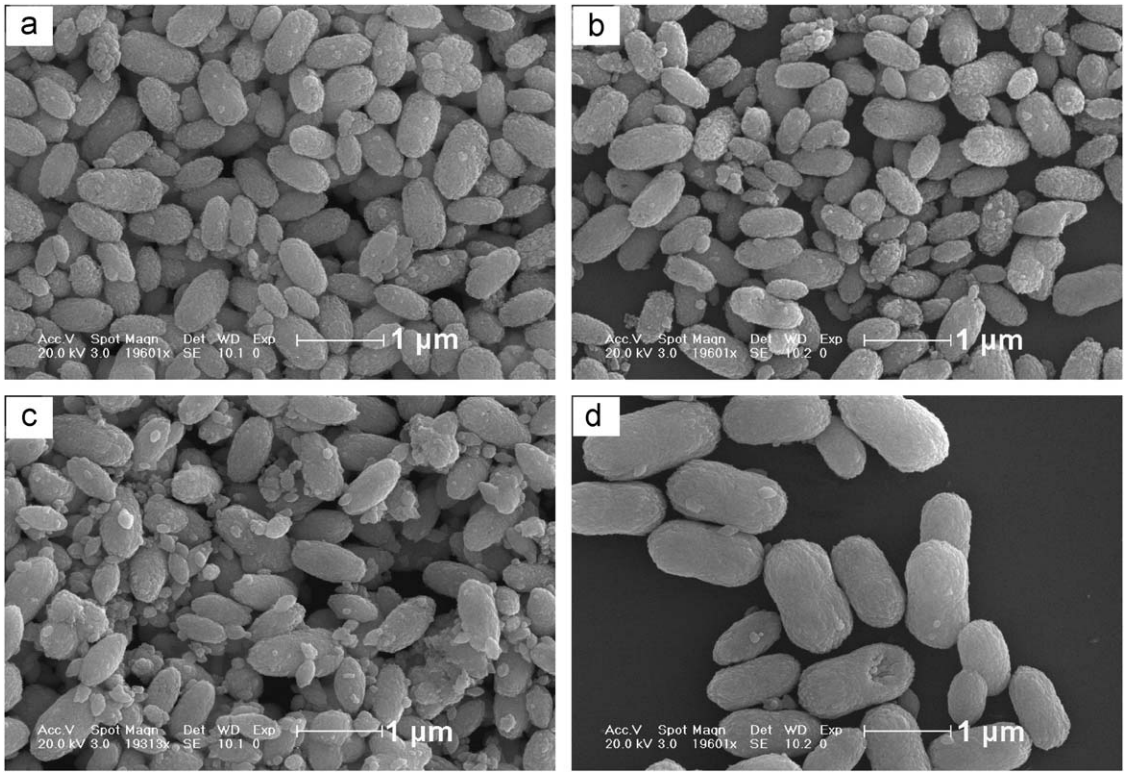

Fig. 10. SEM images of the as-synthesized $BaMoO_4:Eu^{3+}$ particles synthesized at 160 °C for 4 h (a), 8 h (b), 12 (c), and 24 (h).

much similar emission features except for a slight difference in the intensities. In the excitation spectra monitored by the emission of the Tb^{3+} $^5D_4$–$^7F_5$ transition at 544 nm, a broad band from 200 to 400 nm with a maximum at 258 nm can be observed, which can be ascribed to the charge-transfer transitions within the MoO_4^{2-} groups [52]. The f–f transitions within the Tb^{3+} $4f_8$ configuration can hardly be detected due to their weaker intensity with respect to that of MoO_4^{2-}, revealing the efficient energy transfer from MoO_4^{2-} to Tb^{3+}. Upon excitation into the MoO_4^{2-} at 258 nm, the characteristic transition lines from the excited $^5D_4$

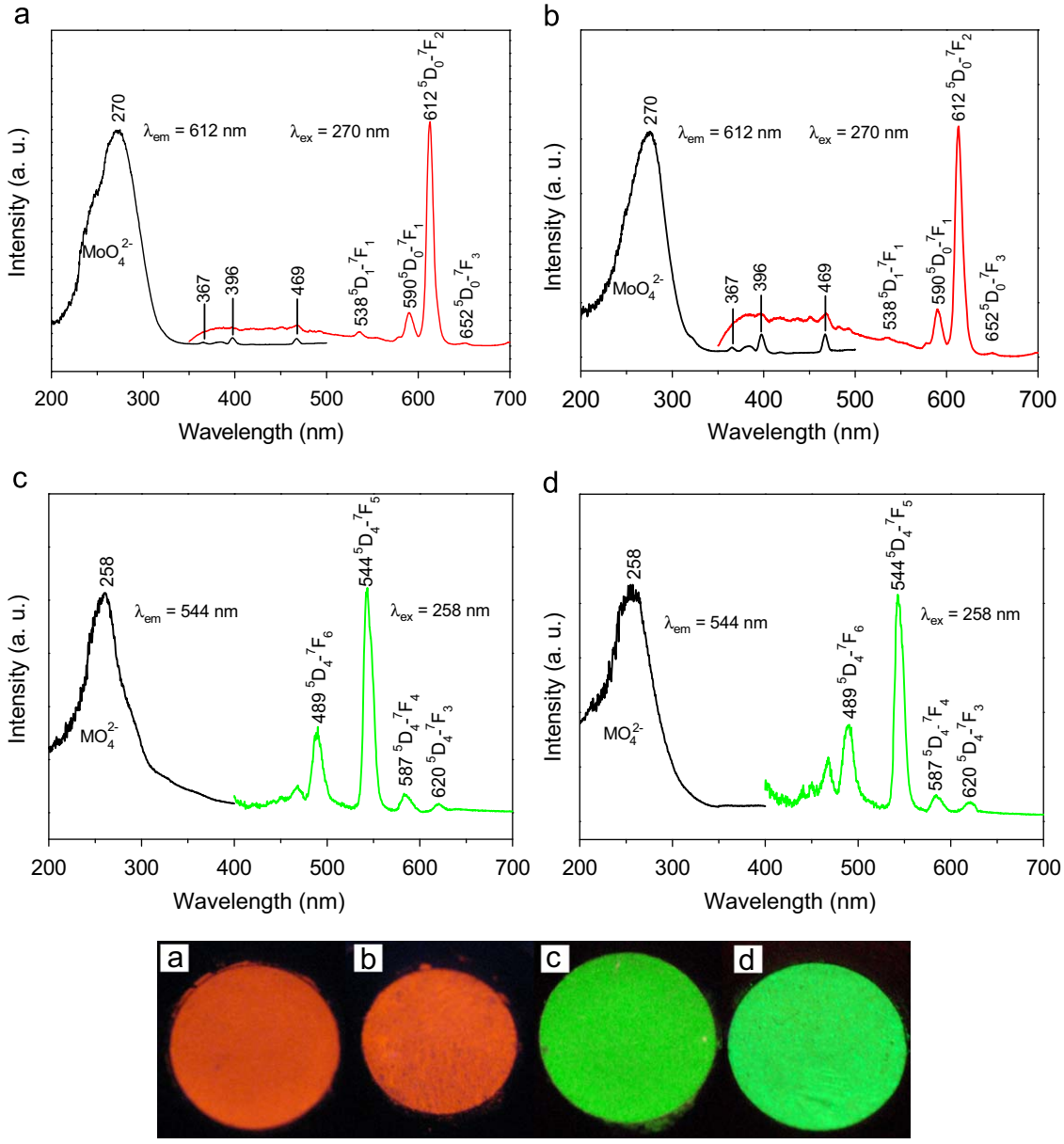

Fig. 11. The excitation (left) and emission (right) spectra for $SrMoO_4:Eu^{3+}$ (a), $BaMoO_4:Eu^{3+}$ (b), $SrMoO_4:Tb^{3+}$ (c), $BaMoO_4:Tb^{3+}$ (d) and their corresponding photographs under ultraviolet (254 nm) excitation.

level of Tb^{3+} are apparent in the emission spectra (Fig. 11c and d, right). Additionally, the characteristic emission of Tb^{3+} with $^5D_4$–$^7F_5$ green emission (544 nm) is the most prominent group compared with other transitions.

The typical decay curves for the luminescence of Eu^{3+} in $AMoO_4:Eu^{3+}$ (A = Sr, Ba) and Tb^{3+} in $AMoO_4:Tb^{3+}$ (A = Sr, Ba) are shown in Fig. 12. It can be seen that the decay curves for $^5D_0$–$^7F_2$ (612 nm) of Eu^{3+} and $^5D_4$–$^7F_5$ (544 nm) of Tb^{3+} can be well fitted into a double-exponential function as $I = A_1 \exp(-t/\tau_1)+A_2 \exp(-t/\tau_2)$ (τ_1 and τ_2 are the fast and slow components of the luminescence lifetimes, A_1 and A_2 are the fitting parameters), and the fitting results are shown in Fig. 12. The respective average lifetimes for $^5D_0$–$^7F_2$ (612 nm) of Eu^{3+} in $SrMoO_4:Eu^{3+}$ and $BaMoO_4:Eu^{3+}$ are 0.71 and 0.55 ms, respectively, which are determined by the formula $\tau = (A_1\tau_1^2+A_2\tau_2^2)/(A_1\tau_1+A_2\tau_2)$ [55]. However, the average lifetimes for $^5D_4$–$^7F_5$ (544 nm) of Tb^{3+} in $SrMoO_4:Tb^{3+}$ and $BaMoO_4:Tb^{3+}$ are 0.99 and 0.88 ms, respectively. The double-exponential decay behavior of the activator is frequently observed when the excitation energy is transferred from the donor to the acceptor [55,56].

4. Conclusions

In summary, rare-earth ion (Eu^{3+}, Tb^{3+}) doped $AMoO_4$ phosphors have been synthesized by a simple solvothermal process using EG as protective agent without further heat treatment. The obtained products exhibit well-defined peanut-like and oval morphologies, non-agglomeration, and narrow size distribution. The obtained $AMo_4:Eu^{3+}$ and $AMoO_4:Tb^{3+}$ phosphors show the characteristic emission lines of Eu^{3+} and Tb^{3+}, respectively. The decay curves of all the samples fit well into a double-exponential function. The possible formation process for the $AMoO_4:Ln$ phosphors has been studied in detail. The solvothermal reaction temperature, reaction time, and EG/H_2O volume ratio play significant roles in the morphologies and sizes of the

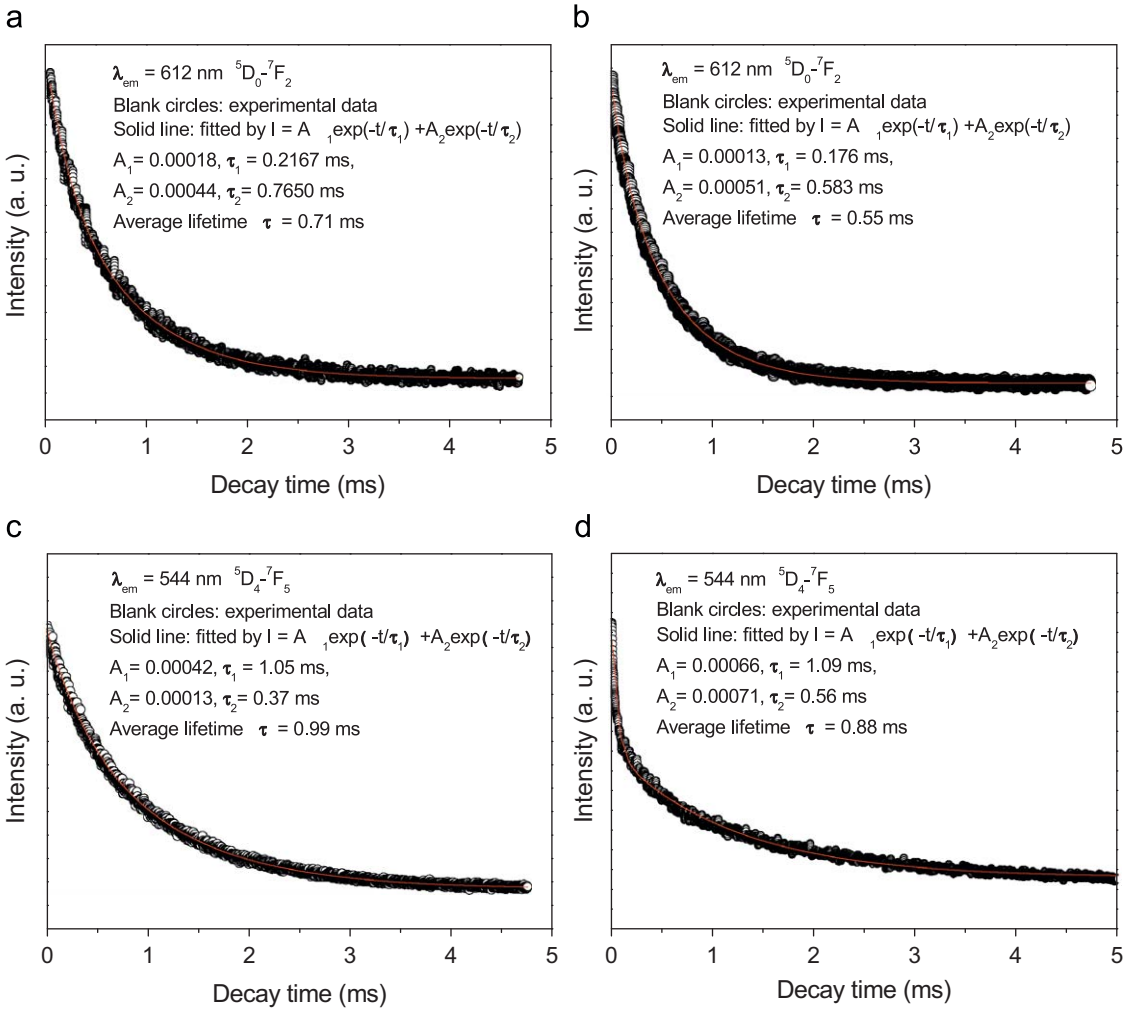

Fig. 12. The decay curves for $SrMoO_4:Eu^{3+}$ (a), $BaMoO_4:Eu^{3+}$ (b), $SrMoO_4:Tb^{3+}$ (c), and $BaMoO_4:Tb^{3+}$ (d).

as-synthesized products. These phosphors exhibit a potential application in the display fields because of their special size, morphology and luminescence properties.

Acknowledgments

This project was financially supported by National Basic Research Program of China (2007CB935502, 2010CB327704), the National Natural Science Foundation of China (NSFC 20871035, 50702057, 50872131), and China Postdoctoral Special Science Foundation (200808281).

References

[1] W. Schartl, Adv. Mater. 12 (2000) 1899.
[2] F. Caruso, Adv. Mater. 13 (2001) 11.
[3] V.A. Suryanarayanan, S. Nair, R.T.J. Tom, Mater. Chem. 14 (2004) 2661.
[4] S.J. Oldenberg, R.D. Averitt, S.L. Westcott, N.J. Halas, Chem. Phys. Lett. 288 (1998) 243.
[5] L.M. LizMarzan, M. Giersig, P. Mulvaney, Langmuir 12 (1996) 4329.
[6] A.P. Alivisatos, Science 271 (1996) 933.
[7] J. Hu, T.W. Odom, C.M. Lieber, Acc. Chem. Res. 32 (1999) 435.
[8] C.N.R. Rao, G.U. Kulkarni, P.J. Thomas, P.P. Edwards, Chem. Eur. J. 8 (2002) 29.
[9] R.A. Caruso, M. Antonietti, Chem. Mater. 13 (2001) 3272.
[10] J. Yang, Z.W. Quan, D.Y. Kong, X.M. Liu, J. Lin, J. Cryst. Growth Des. 7 (2007) 730.
[11] Z.H. Jiang, C.Y. Liu, J. Phys. Chem. B 107 (2003) 12411.
[12] M.S. Fleming, T.K. Mandal, D.R. Walt, Chem. Mater. 13 (2001) 2210.
[13] F. Caruso, M. Spasova, V. Salgueirno-Maceria, Adv. Mater. 13 (2001) 1090.
[14] Q. Lu, F. Gao, S. Komarneni, J. Am. Chem. Soc. 126 (2004) 54.
[15] D.L. Wang, F. Qian, C. Yang, Z.H. Zhong, C.M. Lieber, Nano Lett. 4 (2004) 871.
[16] N.N. Zhao, L.M. Qi, Adv. Mater. 18 (2006) 359.
[17] G. Zhou, M. Lu, Z. Xiu, S. Wang, H. Zhang, Y. Zhou, S.J. Wang, Phys. Chem. B 110 (2006) 6543.
[18] M. Aizawa, A.M. Cooper, M. Malac, J.M. Buriak, Nano Lett. 5 (2005) 815.
[19] D. Kuang, A. Xu, Y. Fang, H. Liu, C. Frommen, D. Fenske, Adv. Mater. 15 (2003) 1747.
[20] M. Wirtz, M. Parker, Y. Kobayashi, C.R. Martin, Chem. Eur. J. 8 (2002) 3572.
[21] C.H. Liu, J.A. Zapien, Y. Yao, X.M. Meng, C.S. Lee, S.S. Fan, Y. Lifshitz, S.T. Lee, Adv. Mater. 15 (2003) 838.
[22] J.Y. Lao, J.Y. Huang, D.Z. Wang, Z.F. Ren, Nano Lett. 3 (2003) 235.
[23] S. Kwan, F. Kim, J. Akana, P.D. Yang, Chem. Commun. (2001) 447.
[24] F. Kim, S. Kwan, J. Akana, P.D. Yang, J. Am. Chem. Soc. 123 (2001) 4360.
[25] J.P. Ge, Y.D. Li, Adv. Funct. Mater. 14 (2004) 157.
[26] M. Zhang, S. Lenhert, M. Wang, L. Chi, N. Lu, H. Fuchs, N. Ming, Adv. Mater. 16 (2004) 409.
[27] S.H. Yu, B. Liu, M.S. Mo, J.H. Huang, X.M. Liu, Y.T. Qian, Adv. Funct. Mater. 13 (2003) 639.
[28] E.F. Paski, M.W. Blades, Anal. Chem. 60 (1988) 1224.
[29] P.G. Zverev, Phys. Status Solidi C 1 (2004) 3101.
[30] D. Errandonea, R.S. Kumar, X. Ma, C. Tu, J. Solid State Chem. 181 (2008) 355.
[31] V. Panchal, N. Garg, A.K. Chauhan, Sangeeta, S.M. Sharma, Solid State Commun. 130 (2004) 203.
[32] D. Errandonea, F.J. Manjon, Prog. Mater. Sci. 53 (2008) 711.
[33] G. Ahmad, M.B. Dickerson, B.C. Church, Y. Cai, S.E. Jones, R.R. Naik, J.S. King, C.J. Summers, N. Kröger, K.H. Sandhage, Adv. Mater. 18 (2006) 1759.
[34] S.E. Harris, S.T.K. Nieh, Appl. Phys. Lett. 17 (1970) 223.
[35] W. Streifer, P. Saltz, IEEE J. Quantum Electron. 9 (1973) 563.
[36] I.C. Chang, P. Katzka, J. Jacob, S. Estrin, IEEE Ultrason. Symp. (1979) 40.
[37] A.A. Kaminskii, S.N. Bagaev, K. Ueda, K. Takaichi, H.J. Eichler, Crystallogr. Rep. 47 (2002) 653.

[38] K. Teshima, K. Yubuta, S. Sugiura, Y. Fujita, T. Suzuki, M. Endo, T. Shishido, S. Oishi, Cryst. Growth Des. 6 (2006) 1598.
[39] V.B. Mikhailik, H. Kraus, G. Miller, M.S. Mykhaylyk, D. Wahl, J. Appl. Phys. 97 (2005) 083523.
[40] L.B. Barbosa, D.R. Ardila, C. Cusatis, J.P. Andreeta, J. Cryst. Growth 235 (2002) 327.
[41] D. Chen, K. Tang, F. Li, H. Zheng, Cryst. Growth Des. 6 (2006) 247.
[42] J.H. Ryu, J.-W. Yoon, C.S. Lim, W.-C. Oh, K.B. Shim, J. Alloy Compd. 390 (2005) 245.
[43] Y. Liu, Y. Chu, Mater. Chem. Phys. 92 (2005) 59.
[44] F. Lei, B. Yan, J. Solid State Chem. 181 (2008) 855.
[45] C. Zhang, E. Shen, E. Wang, Z. Kang, L. Gao, C. Hu, L. Xu, Mater. Chem. Phys. 96 (2006) 240.
[46] Q. Gong, X.F. Qian, X.D. Ma, Z.K. Zhu, Cryst. Growth Des. 6 (2006) 1821.
[47] Z.H. Li, J.M. Du, J.L. Zhang, ;T.C. Mu, Y.N. Gao, B.X. Han, J. Chen, J.W. Chen, Mater. Lett. 59 (2005) 64.
[48] M.D. Barnes, A. Mehta, T. Thundat, R.N. Bhargava, V. Chabra, B. Kulkarni, J. Phys. Chem. B 104 (2000) 6099.
[49] G. Blasse, B.C. Grabmaier, Springer, Berlin, 1994.
[50] G.Z. Li, Z.L. Wang, Z.W. Quan, C.X. Li, J. Lin, Cryst. Growth Des. 7 (2007) 1797.
[51] J.C. Sczancoski, L.S. Cavalcante, M.R. Joya, J.W.M. Espinosa, P.S. Pizani, J.A. Varela, E. Longo, J. Colloid Interf. Sci. 330 (2009) 227.
[52] J.A. Groenink, C. Hakfoort, G. Blasse, Phys. Status Solidi A 54 (1979) 329.
[53] C.X. Li, Z.W. Quan, J. Yang, P.P. Yang, J. Lin, Inorg. Chem. 46 (2007) 6329.
[54] D.L. Shi, J. Lian, W. Wang, G.K. Liu, P. He, Z.Y. Dong, Adv. Mater. 18 (2006) 189.
[55] S. Mukarami, H. Markus, R. Doris, M. Makato, Inorg. Chim. Acta 300 (2000) 1014.
[56] C. Hsu, R.C. Poweh, J. Lumin. 10 (1975) 273.